Inorganic Chemistry
Article
pubs.acs.org/IC

Understanding the Mechanism of Polymerization of ε-Caprolactone Catalyzed by Aluminum Salen Complexes

Maria O. Miranda, Yvonne DePorre, Hugo Vazquez-Lima, Michelle A. Johnson, Daniel J. Marell, Christopher J. Cramer,* and William B. Tolman*

Department of Chemistry, Center for Sustainable Polymers, Chemical Theory Center, and Supercomputing Institute, University of Minnesota, 207 Pleasant Street SE, Minneapolis, Minnesota 55455, United States

Ⓢ *Supporting Information*

ABSTRACT: Studies of the kinetics of polymerization of *ε*-caprolactone (CL) by salen-aluminum catalysts comprising ligands with similar steric profiles but different electron donating characteristics (R = OMe, Br, or NO_2) were performed using high initial monomer concentrations ($2\ M < [CL]_0 < 2.6\ M$) in toluene-d_8 at temperatures ranging from 20 to 90 °C. Saturation behavior was observed, enabling determination of monomer equilibrium constants (K_{eq}) and catalytic rate constants (k_2) as a function of R and temperature. While K_{eq} varied only slightly with the electron donating properties of R (Hammett $\rho = +0.16(8)$), k_2 showed a more significant dependence reflected by $\rho = +1.4(1)$. Thermodynamic parameters $\Delta G°$ (associated with K_{eq}) and $\Delta G^\ddagger$ (associated with k_2) were determined, with the former being ~0 kcal/mol for all catalysts and the latter exhibiting the trend R = OMe > Br > NO_2. Density functional theory (DFT) calculations were performed to characterize mechanistic pathways at a microscopic level of detail. Lowest energy transition-state structures feature incipient bonding of the nucleophile to the lactone carbonyl that is approaching the metal ion, but a distinct CL adduct is *not* an energy minimum on the reaction pathway, arguing against K_{eq} being associated with coordination of monomer according to the typical coordination−insertion mechanism. An alternative hypothesis is presented associating K_{eq} with "nonproductive" coordination of substrate in a manner that *inhibits* the polymerization reaction at high substrate concentrations.

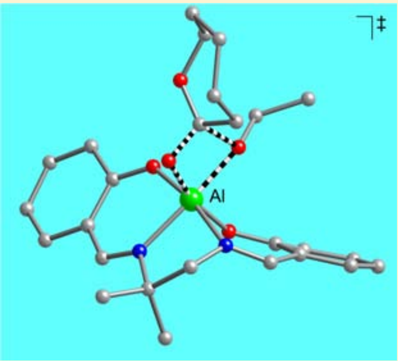

INTRODUCTION

Ring-opening transesterification polymerization (ROTEP, a specific type of ring-opening polymerization) of cyclic esters is an important method for converting renewable resources to aliphatic polyesters, sustainable materials useful for myriad applications and as potential alternatives to petrochemical polymers.[1] Polymerization of monomers like lactide (LA) and *ε*-caprolactone (CL) have been particularly well studied using a variety of polymerization methods.[2] Metal-alkoxide catalysts are often employed as ROTEP catalysts in both academic and industrial settings, and are especially attractive because of their ability to generate high molecular weight polymers in controlled fashion, with low polydispersities, and with maintenance of end-group fidelity.[2a−d]

The mechanistic paradigm for ROTEP by single-site metal alkoxide catalysts is the so-called "coordination−insertion" pathway (Figure 1). According to this mechanism, monomer coordinates through the carbonyl oxygen to a vacant site on the Lewis acidic metal, followed by alkoxide insertion into the activated carbonyl carbon and ring-opening to generate a new propagating alkoxide. While widely accepted, significant gaps in our understanding of this mechanism remain. For example, variable electronic and steric effects of supporting ligands on rates of ROTEP catalyzed by metal alkoxide complexes raise questions about the relative importance of monomer binding, alkoxide nucleophilicity, or both in controlling polymerization reactivity. Thus, for various salen aluminum catalysts, the groups of Gibson and Nomura both observed increased rates for the polymerization of LA when the ligands were substituted with electron-withdrawing groups (EWGs).[3,4] They postulated the enhancement is due to increased Lewis acidity of the aluminum, which boosts monomer binding and activation. Another study using a dinuclear salen aluminum complex found contradictory rate trends between monomers; in the case of LA polymerization, EWGs increased the rate, whereas in the case of CL polymerization, the opposite effect was observed.[5] Rate attenuation by EWGs has also been observed for titanium salen complexes,[6] magnesium complexes bearing benzenesulfonate phenol ligands,[7] and some aluminum alkoxide complexes supported by bis(phenolate)diamine ligands (**1**).[8]

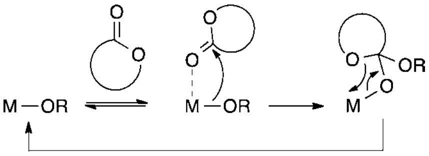

Figure 1. Coordination−insertion mechanism for the polymerization of cyclic esters.

Received: September 4, 2013
Published: November 12, 2013

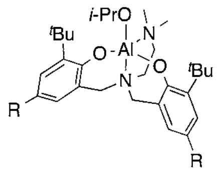

1

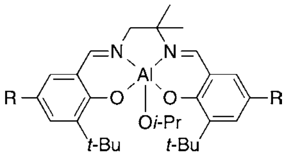

2

R = OMe, Br, NO_2

We recently examined the kinetics of CL polymerization catalyzed by the latter aluminum alkoxide complexes (**1**) in detail.[9] We found that by studying the reactions using high concentrations of monomer, saturation kinetics were observed, enabling determination of a monomer binding equilibrium constant, K_{eq}, and a catalytic rate constant, k_2, that we attributed to the coordination and insertion steps, respectively. The data showed that the origin of the rate differences across the series of catalysts is entirely due to differences in k_2, and on the basis of both experiment and theory we argued that the nucleophilicity of the alkoxide is the determining factor (increasing nucleophilicity with increasing electron-donation). However, analysis of the catalytic activity of **1** was complicated by the potential for decoordination of the dimethylalkylamino arm of the polydentate ligand.

With the aim of further understanding the diverse electronic and steric effects of ligand substituents on the ROTEP efficiencies of metal alkoxide complexes, we turned our attention to aluminum complexes supported by salen-type ligands (**2**), where decoordination of the ligand from the metal ion is unlikely. Such Schiff base complexes have been used extensively in catalysis,[10] and (with variable substituents and linkers between the imino nitrogen atoms) are notably effective for ROTEP of a variety of lactones.[3,4,11−24] Published kinetic/mechanistic studies of ROTEP catalyzed by Schiff base Al compounds have provided important information, such as ligand structural effects on ROTEP rates for a variety of lactones[23] (cf. the aforementioned rate enhancement of LA polymerization by electron withdrawing ligand substituents),[3,4] ^{1}H NMR spectroscopic evidence for reversible LA coordination to the catalyst,[21] and the basis for observed poly(lactide) (PLA) tacticity in stereospecific polymerizations.[12−16,20,21]

Herein we report the results of detailed kinetic studies of CL polymerization by well-characterized, monomeric aluminum salen complexes with identical steric profiles but variable remote substituents with differing electron donating characteristics (**2**). Using our previously described methodology involving ^{1}H NMR spectroscopic analysis of ROTEP kinetics performed with high initial monomer concentrations,[9] we again observed saturation behavior that enabled determination of K_{eq} and k_2 values for the catalyst series **2**, but with trends opposite to that seen for **1**. Density functional theory (DFT) calculations were performed to rationalize the kinetic data, and provided key mechanistic insights, including a new rationale for the experimental rate law that has significant, broader implications for evaluating metal-alkoxide catalyzed ROTEP kinetics.

■ RESULTS AND DISCUSSION

Synthesis and Characterization of Ligands and Catalysts. The ligands required to synthesize complexes **2** (R = OMe, Br, NO_2) were prepared using a traditional imine condensation between the three differently substituted salicylaldehydes and 2-methylpropane-1,2-diamine in yields ranging from 35% (R = Br) to 98% (R = OMe). Complexes **2** were synthesized in high yields (84−97%) via thermolysis of equimolar amounts of ligand and aluminum tris(*iso*-propoxide) in toluene. Complexes **2** (R = Br, NO_2) were isolated as analytically pure yellow and light brown solids, respectively, directly from the reaction mixture, whereas **2** (R = OMe) required recrystallization from toluene and pentane to isolate pure, bright yellow, material. The compounds are air- and moisture-sensitive and soluble in chlorinated (dichloromethane) and aromatic hydrocarbon (toluene) solvents. As in the case of their ligands, the catalysts have similar features in their ^{1}H NMR spectra, with the most significant differences being in the aryl region; the aryl residues shift downfield as the electron-withdrawing nature of the catalyst increases. In solution the complexes appear monomeric, as expected because of the presence of the *t*-butyl substituents[25] and as indicated by a single set of resonances in their ^{1}H NMR spectra and a single resonance in their ^{27}Al NMR spectra at 35, 34, and 33 ppm (R = OMe, Br, or NO_2, respectively). This ^{27}Al NMR chemical shift region is indicative of a five-coordinate aluminum center, and matches that reported previously for a pentacoordinate salen-type aluminum alkoxide (35 ppm).[16,18,26]

In addition, a crystal of **2** (R = OMe) suitable for X-ray diffraction was obtained from a toluene/hexane mixture at −40 °C. The structure (Figure 2) features a monomeric complex with a 5-coordinate aluminum ion in a geometry between square pyramidal and trigonal bipyramidal ($\tau = 0.52$).[27] Other structures of complexes with the 2-methylpropane-1,2-diamine backbone display similarly intermediate τ parameters ($0.48 < \tau < 0.56$).[3,25] Bond distances and angles are consistent with other aluminum salen-type structures.

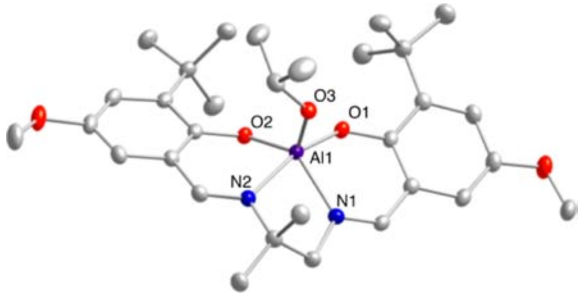

Figure 2. Representation of the X-ray crystal structure of **2** (R = OMe), showing nonhydrogen atoms as 50% thermal ellipsoids. Selected interatomic distances (Å) and angles (deg): Al1−O1, 1.8107(13); Al1−O2, 1.7899(12); Al1−O3, 1.7292(13); Al1−N1, 2.0042(14); Al1−N2, 2.0445(15); O3−Al1−O2, 115.98(6); O3−Al1−O1, 100.22(6); O2−Al1−O1, 97.57(6); O3−Al1−N1, 113.60(6); O2−Al1−N1, 129.72(6); O1−Al1−N1, 87,59(6); O3−Al1−N2, 96.96(6); O2−Al1−N2, 88.00(6); O1−Al1−N2, 161.05(6); N1−Al1−N2, 78.22(6).

Polymerization Kinetics. Polymerizations of CL using catalysts **2** were performed in triplicate with fixed initial concentrations of CL ($2\ \text{M} < [\text{CL}]_0 < 2.6\ \text{M}$) and catalyst ($5.5\ \text{mM} < [\mathbf{2}]_0 < 7\ \text{mM}$) in toluene-$d_8$ at temperatures ranging from 20 to 90 °C. As in a previous study,[9] features due to the growth of polymer and decay of monomer were monitored by ^{1}H NMR spectroscopy to polymerization completion (conversions >99%) and their concentrations as a function of time were fit to the Michaelis−Menten expression (eq 1) using the global kinetics fitting program COPASI (version 4.8).[28] Good agreement between the fit and the data was obtained (representative plot in Figure 3; all data shown in Supporting

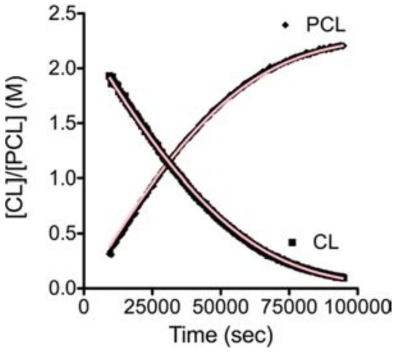

Figure 3. Illustrative conversion vs. time profile for decay of CL (■) and growth of PCL (♦) resonances during ROTEP catalyzed by R = OMe at 333 K, determined from ^{1}H NMR spectra, along with fits (red lines) determined by COPASI.

Information, Figure S1. These fits, and curved rate vs. [CL] plots derived from both the COPASI analysis (Supporting Information, Figure S2) and a reaction progress kinetic analysis[29] (using derivatives of polynomial fits; Supporting Information, Figure S7) support saturation behavior; significantly poorer fits were obtained using simpler first- or second-order rate equations (Supporting Information, Figures S3−S7). Average values from replicate runs for K_{eq} and k_2 are listed in Table 1, with all values provided in Supporting Information, Table S1. In addition, independent measurements of K_{eq} were obtained by analyzing observed changes in the chemical shift of the aryl and imine catalyst residues (Figure 4) as a function of time and [CL], using eq 2[9] (fits shown in Supporting Information, Figure S8−S10). Comparison of these K_{eq} values with those obtained from the averaged COPASI fits shows reasonable agreement between the independently calculated parameters (Table 1), providing further evidence for the validity of eq 1. The data are thus consistent with the typical kinetic model associated with eq 1 involving pre-equilibrium monomer binding followed by insertion, but other kinetic models described by eq 1 are also possible (vide infra).

Table 1. Average Values of Kinetic Parameters Determined from COPASI Fits and NMR Peak Analysis

entry	temp (K)	R	K_{eq} COPASI (M^{-1})	K_{eq} NMR (M^{-1})	k_2 (s^{-1}) ($\times 10^2$)
1	333	OMe	0.9(1)	0.70(5)	1.00(3)
2	343	OMe	0.92(9)	0.54(7)	2.1(1)
3	353	OMe	0.86(3)	0.56(5)	3.8(1)
4	363	OMe	0.7(1)	0.50(7)	5.9(1)
5	313	Br	1.38(8)	0.83(6)	1.39(8)
6	323	Br	1.19(5)	0.8(1)	2.7(1)
7	333	Br	1.37(6)	0.76(4)	4.3(2)
8	343	Br	1.16(2)	0.64(5)	7.9(6)
9	293	NO_2	1.64(5)	2.2(3)	2.34(6)
10	303	NO_2	1.5(1)	1.7(2)	5.2(5)
11	313	NO_2	1.66(7)	1.7(3)	8.0(4)
12	323	NO_2	1.45(4)	1.5(1)	15.4(8)

$$-\frac{d[CL]}{dt} = \frac{d[PCL]}{dt} = \frac{k_2[\mathbf{2}][CL]}{1/K_{eq} + [CL]} \tag{1}$$

$$\Delta\delta = \Delta\delta_{uncoord} + \frac{(\Delta\delta_{uncoord} - \Delta\delta_{coord})[CL]}{K_M + [CL]} \tag{2}$$

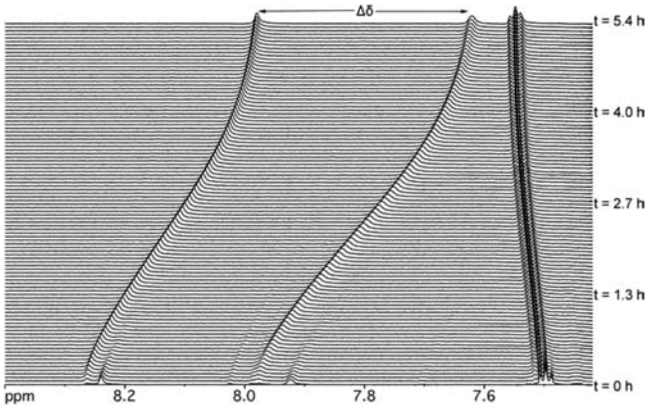

Figure 4. Portion of the ^{1}H NMR spectra acquired during polymerization of CL by **2** (R = Br) at 333 K illustrating how the aryl resonances for the complex in solution change as a function of reaction time. The indicated peak separation $\Delta\delta$ was used to independently evaluate K_{eq} (see eq 2). Note the conversion of the catalyst during early reaction times (t = 0−1 h) that is modeled in Supporting Information, Figure S11.

An induction period was seen in the kinetic runs, as had been noted previously for ROTEP by related aluminum systems, and close inspection of ^{1}H NMR spectra revealed transformations of the catalyst during these early reaction times (cf. t = 0 to 1.3 h in Figure 4). The initial ^{1}H NMR spectrum obtained soon after mixing of the catalyst with CL contained imine peaks different from those of the catalyst in the absence of CL, suggesting some rapid change of the catalyst structure in the presence of substrate. In addition, these peaks smoothly converted to a second set of peaks as polymerization began. This conversion follows first order kinetics, with a rate that is similar to the rate of polymerization (Supporting Information, Figure S11). The NMR data suggest structural changes to the catalyst and/or precatalyst, possibly including binding of monomer, initiation via isopropoxide insertion, or some other geometric change, but definitive conclusions cannot be drawn with the information currently available.

Interpretation of Kinetic Parameters. We evaluated the dependencies of K_{eq} and k_2 on the catalyst R group and temperature through Hammett, Eyring, and van't Hoff plots, with the aim of discerning electronic effects and obtaining thermodynamic parameters (Figure 5). Turning first to K_{eq}, we find only very weak dependencies on substituent and temperature from plots of log(K_{eq}) vs. σ_p (Figure 5a, red)[30,31] and ln(K_{eq}) vs. $1/T$ (Figure 5b), respectively. A linear relationship between log(K_{eq}) and σ_p with a small positive slope ρ (average = +0.16(8)) indicates that the equilibrium constant for monomer binding is slightly enhanced by EWGs, in line with previous explanations for the reactivity of aluminum salen complexes.[3] However, this effect is small, which is highlighted by the small differences in the $\Delta G°$ values (Table 2) calculated from Figure 5b (e.g., the $\Delta\Delta G°$ between **2** with R = OMe and R = Br at 333K is less than 0.4 kcal/mol). For all catalysts studied, $\Delta G°$ values are zero within experimental error. Importantly, the small differences in K_{eq} and $\Delta G°$ as a function of substituents cannot fully explain the differences in the observed overall rates for this set of catalysts.

The dependencies of k_2 on substituent R and temperature are more striking (Figure 5a,c), and show that the overall rate differences between the ROTEP polymerizations by catalysts **2** arise from this kinetic parameter. Linear relationships between

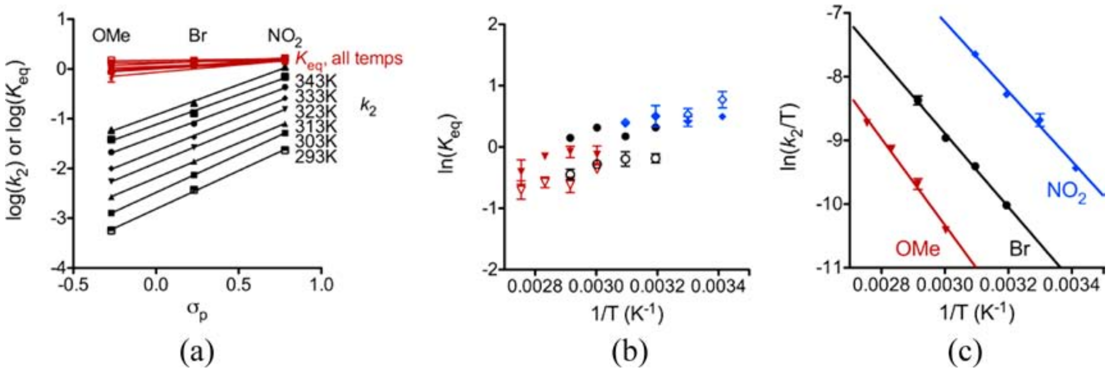

Figure 5. (a) Hammett plot for k_2 (black) and K_{eq} (red). (b) van't Hoff plot for K_{eq} (R = OMe, red triangles; R = Br, black circles; R = NO_2, blue diamonds). Closed points denote equilibrium constant values determined by COPASI; open points denote values determined by NMR peak analysis method. (c) Eyring plot for k_2 values.

Table 2. Thermodynamic Parameters Associated with K_{eq} for Catalysts 2 Determined by COPASI and NMR Peak Analysis

R	method	$\Delta H°$ (kcal/mol)	$\Delta S°$ (cal/mol K)	$\Delta G°$ (kcal/mol, 323 K)
OMe	COPASI	−2.1 ± 0.9	−7 ± 3	−0.03 ± 1
OMe	NMR	−2.3 ± 0.5	−8 ± 2	0.2 ± 0.7
Br	COPASI	−0.8 ± 0.5	−2 ± 1	−0.2 ± 0.6
Br	NMR	−1.8 ± 0.3	−6 ± 1	0.2 ± 0.5
NO_2	COPASI	−0.5 ± 0.3	−0.8 ± 1	−0.2 ± 0.5
NO_2	NMR	−2.2 ± 0.4	−6 ± 1	−0.2 ± 0.6

log(k_2) and the σ_p values at all temperatures have similar positive slopes (ρ) with an average value of +1.4(1). The linear correlations support a similar mechanism(s) across the series of catalysts, and the positive ρ values reflect enhancement of k_2 with increasing substituent electron withdrawing power. This trend is notably opposite from that reported previously for catalysts **1** ($\rho = -1.1(1)$).[9] Further insight is provided by the activation parameters calculated using the Eyring equation from Figure 5c (Table 3). A clear trend in both the activation enthalpy and Gibb's free energy of activation that mimics the overall rate order is observed, albeit with no discernible trend in the activation entropies (within error). The modest positive activation enthalpies accompanied by negative activation entropies imply a degree of bond breaking and ordering in the transition state consistent with the insertion process, with further understanding made available from DFT calculations (see below).

Table 3. Activation Parameters for k_2

R	$\Delta H^{\ddagger}$ (kcal/mol)	$\Delta S^{\ddagger}$ (cal/mol K)	$\Delta G^{\ddagger}$ (kcal/mol, 323 K)
OMe	13.5 ± 0.5	−27 ± 2	22.3 ± 0.8
Br	11.5 ± 0.3	−30 ± 2	21.3 ± 0.7
NO_2	10.8 ± 0.4	−29 ± 2	20.2 ± 0.8

Density Functional Modeling. *(a). Pathway Analysis on Models Lacking para Substituents.* To characterize in microscopic detail the various elementary steps associated with the ROTEP mechanism, we began by applying a DFT model that has been extensively validated for organic and main-group inorganic systems (M06-2X/6-311+G(d,p)//M06-L/6-31+G(d,p) including toluene solvation effects using a quantum chemical continuum model; see Computational Methods section for full details) to a truncated model catalyst from which bulky alkyl substituents were removed (and isopropoxide truncated to methoxide) to facilitate initial identification of important stationary-point structures (denoted **r**, Figure 6).[32]

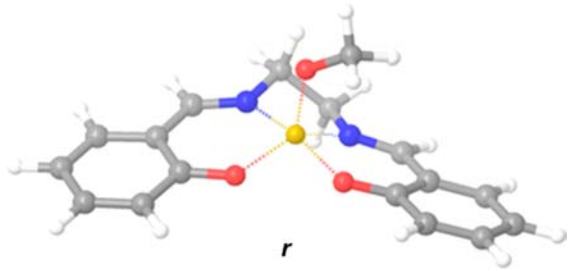

Figure 6. Truncated model **r** for catalysts **2**.

Many complexes of **r** with CL can be found and identified as minima on the potential energy surface (PES). These include van der Waals complexes, with CL "stacking" above or below an aromatic ring, and various structures coordinating either of the two ester oxygen atoms of CL to the aluminum atom. However, while all of these structures are minima on the potential energy surface, they are all predicted to have positive free energies relative to separated reactants, such that product distributions would be expected to follow the Curtin−Hammett principle. As a result, we will therefore begin with a focus primarily on transition-state (TS) structures and their energies. Later, however, we will return to the myriad of catalyst·CL complexes to rationalize what we believe to be substrate-inhibition effects in the observed kinetics.

As noted above, the calculations indicate that monomer coordination to aluminum does *not* generate a significantly stable intermediate that precedes a separate insertion step, (as is often assumed, cf. Figure 1). Nonetheless, the alkoxide and CL must indeed be brought into proximity to accomplish the alkoxide insertion step. Consideration of this step leads to eight stereochemically distinct and mechanistically productive insertion orientations of the alkoxide and CL relative to the catalyst structure. These eight orientations (Figure 7) differ in the orientation of the CL monomer and the orientation of the noncoordinated oxygen (carbonyl or ester) relative to the nitrogen ligands (*trans*/*trans*, *trans*/*cis*, *cis*/*trans*, and *cis*/*cis*) as well as whether coordination occurs through the monomer carbonyl or ester oxygen atom ($O_{carbonyl}$ and O_{ester}, respectively).

The ring-opening polymerization proceeds via two distinct mechanistic routes depending on how CL coordinates to the Al

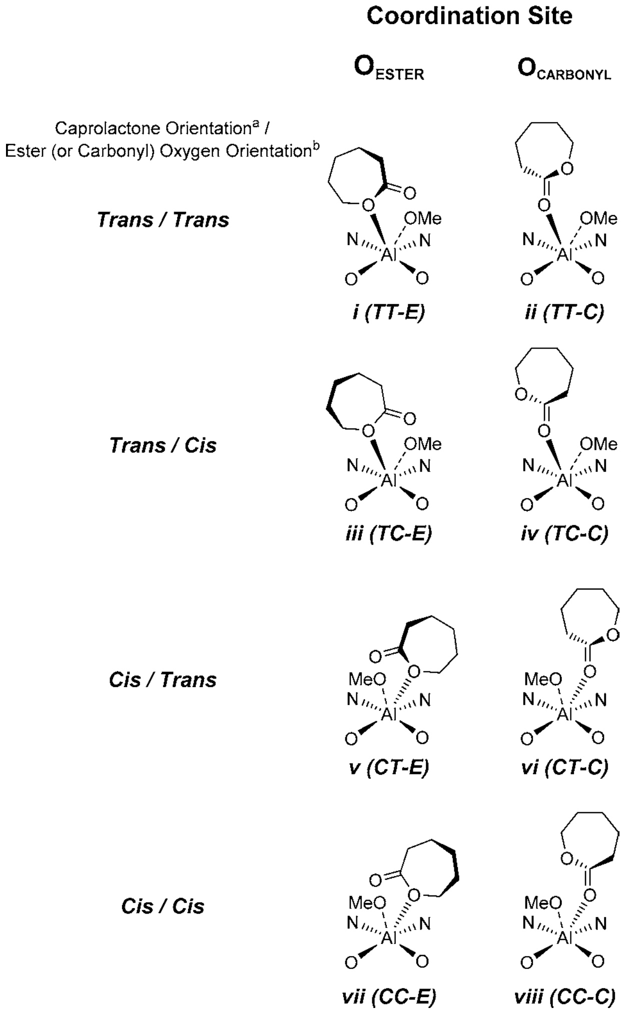

Figure 7. Eight distinct CL **r** complex structures from which alkoxide insertion may proceed; complete geometries are provided in the Supporting Information. [a]Orientation of the CL is given relative to the nitrogen ligands. [b]Orientation of the ester or carbonyl oxygen is given relative to the nitrogen donors.

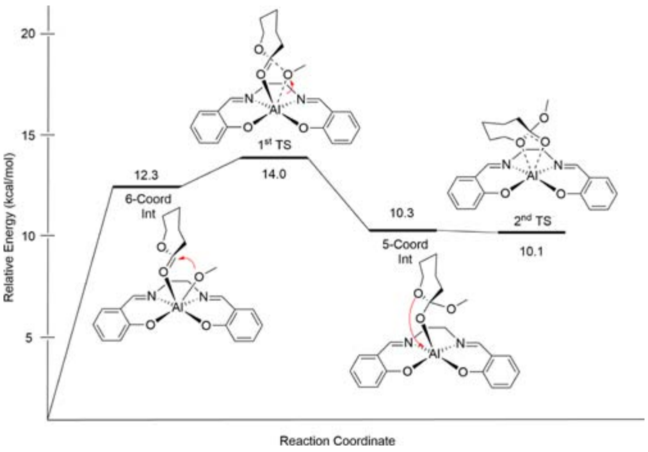

Figure 8. Reaction path for **r**-*vi*; this path is computed to have the lowest activation free energy of eight distinct stereochemical possibilities shown in Figure 8.

Table 4. Free Energies (kcal/mol) Relative to Separated Reactants for Reaction Paths Involving O_{ester}−Al Coordination in the Truncated r and More Elaborate s Models[a]

orientation	6-coordinate intermediate	TS structure
r-*i*	12.9	16.8
s-*i*	16.7	17.7
r-*iii*	11.8	19.5
s-*iii*	17.6	22.2
r-*v*	16.0	16.7
s-*v*	17.9	17.6
r-*vii*	*b*	19.6
s-*vii*	*b*	20.2

[a]See computational methods section for theoretical details. [b]No stationary point preceding the TS structure could be located.

Table 5. Free Energies (kcal/mol) Relative to Separated Reactants for Reaction Paths Involving $O_{carbonyl}$−Al Coordination in Truncated r and More Elaborate s Models (See Also Figure 8)[a]

orientation	6-coordinate intermediate	1st transition state	5-coordinate intermediate	2nd transition state
r-*ii*	11.4	17.2	9.2	14.8
s-*ii*	*b*	16.5	7.0	15.3
r-*iv*	11.3	19.3	6.9	7.4
s-*iv*	*b*	18.0	6.2	11.3
r-*vi*[c]	**12.3**	**14.0**	**10.3**	**10.1**
s-*vi*[c]	*b*	**14.9**	**10.6**	**12.2**
r-*viii*	8.1	17.3	10.4	15.6
s-*viii*	*b*	17.6	8.7	13.9

[a]See computational methods section for theoretical details. [b]Stationary points were not computed for these structures. [c]This pathway has the lowest rate-limiting activation free energy of the eight stereochemically distinct possibilities.

center along the insertion pathway. Initial approach involving the ester oxygen (*i, iii, v, vii*) provides access to an alkoxide-insertion TS structure from which ring-opened product is directly obtained (Supporting Information, Figure S15). By contrast, initial approach involving the carbonyl oxygen (*ii, iv, vi, viii*) leads to an alkoxide-insertion TS structure that generates a reactive orthoalkoxide intermediate (Figure 8, first TS). Subsequent exchange of the newly generated alkoxide oxygen and the original ester oxygen, with concomitant ring-opening, then proceeds via a second TS structure that leads to ring-opened product.

The relative free energies for the key stationary points on all pathways for the truncated model **r** are listed in Tables 4 and 5 for O_{ester} and $O_{carbonyl}$ coordination, respectively (all structures are provided in Supporting Information; these tables also include data for a more elaborate model **s** including all experimental alkyl substituents described below). The ring-opening pathway associated with ***vi*** (*CT-C*) was found to have the *lowest* activation free energy of all eight possible pathways, 14.0 kcal/mol, with the rate limiting step being the initial alkoxide insertion. Note that the initial 6-coordinate intermediate is 12.3 kcal/mol above separated reactants in free energy, even though it is predicted to be a minimum on the potential energy surface. Also, the orthoalkoxide intermediate is predicted to be a very shallow minimum on the potential energy surface, such that adding thermal contributions to arrive at a free energy leads to the intermediate being effectively degenerate with the second TS structure for ring-opening that generates product alkoxide. As such, the orthoalkoxide is kinetically irrelevant. Cases **r**-*i*, **r**-*ii*, **r**-*v*, and **r**-*viii* have rate-limiting free energies of activation of 15−17 kcal/mol, that is, only slightly above that for **r**-*vi*. In the remaining cases, **r**-*iii*, **r**-*iv*, and **r**-*vii*, steric clashes between the phenyl rings of the Al-salen complex and the CL ring destabilize the rate-determining TS structures leading to activation free energies above 19 kcal/mol.

With results in hand for the eight pathways associated with model **r**, we next examined the influence of the two *t*-butyl and two methyl groups that are present in the experimental salen ligand by introducing them into the computational model, hereafter referred to as model **s**. The mean unsigned difference between the relative free energies for corresponding stationary points of model **r** vs model **s** (Tables 4 and 5) is only 1.8 kcal/mol, indicating that most of the relative energies are not especially perturbed by the additional steric bulk in model **s**. However, all of the structures involving coordination to the *ester* oxygen are *de*stabilized, because these structures bring the CL ring into closer proximity to the steric bulk of the full catalyst model. Indeed, the 6-coordinate intermediate **s**-*iii* is destabilized by 5.8 kcal/mol relative to the truncated ***r*** model owing to unfavorable interactions with the methyl groups on the salen bridge. The looser complexes associated with carbonyl oxygen coordination are by contrast in some cases *stabilized* by favorable dispersion interactions (i.e., attractive London forces at van der Waals contact), for example, the 5-coordinate intermediate **s**-*ii* whose relative energy is 2.2 kcal/mol more stable than that of **r**-*ii*. As might be expected given the small mean unsigned difference between models **r** and **s**, we find that again the lowest energy pathway upon inclusion of the alkyl substitution is pathway ***vi*** (Figure 9), with a rate-limiting free energy of activation of 14.9 kcal/mol, which is slightly increased from the 14.0 kcal/mol value obtained with model **r**.

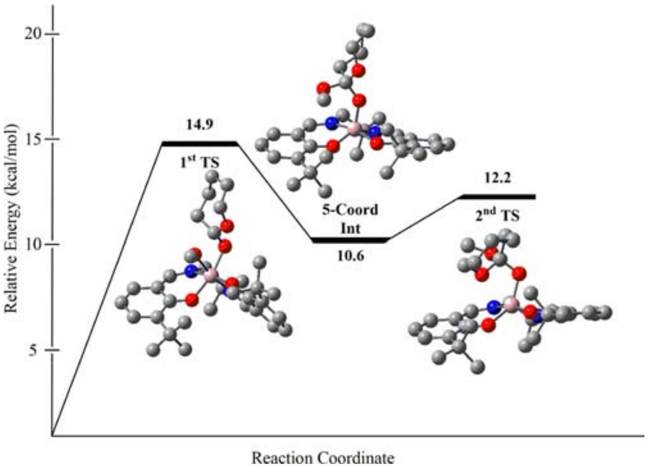

Figure 9. Lowest-energy pathway corresponding to **s**-***vi*** pathway.

(b). Influence of para Substituents on the Reaction Pathways. Having assessed the effect of additional steric bulk in the salen ligand, we examine next the electronic effects observed with *para* substitution. The same eight pathways (***i***–***viii***) were investigated for the **s** model substituted with *p*-MeO, *p*-Br, and *p*-NO_2, corresponding to the experimental systems **2**. In addition, we chose to use ethoxide in place of methoxide to mimic more accurately a growing polymer chain.

There are some general trends to be observed for the ester coordination pathway (Table 6). The lactone-coordinated intermediate is stabilized by substitution at the *para* position for all pathways and substitutions. With increasing electron-withdrawing power of the substituent (OMe < Br < NO_2), the intermediate is further stabilized (mean unsigned difference between the model **s** and each substituent is 1.3, 2.9, and 3.7 kcal/mol respectively), consistent with the increased Lewis acidity of the Al atom that is expected with aryl rings substituted by more EWGs. That increased Lewis acidity may be assessed through the evaluation of the CM5 partial atomic charge[33] of the Al atom, which increases smoothly from 0.535 to 0.538 to 0.544 with the substituent going from MeO to Br to NO_2.

Table 6. Free Energies (kcal/mol) Relative to Separated Reactants for Reaction Paths Involving O_{ester}−Al Coordination in Full *para*-Substituted Models[a]

orientation	6-coordinate intermediate	transition state
***i*-OMe**	14.3	17.4
***i*-Br**	12.4	16.7
***i*-NO_2**	11.6	16.0
***iii*-OMe**	17.7	23.8
***iii*-Br**	15.6	22.0
***iii*-NO_2**	15.8	21.7
***v*-OMe**	16.6	18.3
***v*-Br**	15.6	15.6
***v*-NO_2**	13.6	16.3
***vii*-OMe**	*b*	22.1
***vii*-Br**	*b*	20.3
***vii*-NO_2**	*b*	20.6

[a] See computational methods section for theoretical details. [b] No stationary points preceding the TS structure could be located.

For the subsequent TS structures, the *para*-methoxy substituted compounds show mixed results with some pathways being stabilized and some destabilized, over a range of −0.3 to +1.9 kcal/mol relative to unsubstituted **s** results above (cf. Table 5). In the case of *p*-Br, the range is −2.0 to +0.1, and in the case of *p*-NO_2, it is −1.7 to +0.4. The variability in the *para* substitution effect in these systems may be associated with varying degrees of dissociative character in the separation of the nucleophile alkoxide *from* the aluminum atom (which would be expected to be *disfavored* by EWGs) and associative character of the newly formed alkoxide *to* the aluminum atom (which would be *favored* by the same EWGs). The varying geometries associated with each path permit such differentiation. However, as the free energies of activation in Table 6 considerably exceed those associated with carbonyl coordination (vide infra) we will not explore these trends further.

Consistent with the results for the **r** and **s** models above, pathway ***vi*** in the carbonyl coordination pathway case was found to have the lowest rate-limiting free energy of activation (Table 7), and to show a trend in relative activation free energies relative to *p*-MeO of −1.2 for *p*-Br, and −2.8 for *p*-NO_2. These free energy differences are in agreement with those measured (−1.0 ± 1.1 and −2.1 ± 1.1, respectively; derived from Table 4) to within experimental uncertainty. Analysis of the geometries along pathway ***vi*** indicates that substitution with

Table 7. Free Energies (kcal/mol) Relative to Separated Reactants for Reaction Paths Involving $O_{carbonyl}$–Al Coordination in Full *para*-Substituted Models[a]

orientation	1st transition state	5-coordinate intermediate	2nd transition state
ii-OMe	21.7	8.9	17.1
ii-Br	21.9	8.3	13.5
ii-NO$_2$	18.4	9.0	15.1
iv-OMe	19.2	6.3	11.1
iv-Br	20.2	6.2	14.5
iv-NO$_2$	19.0	5.3	9.2
vi-OMe[b]	**14.3**	**11.5**	**12.3**
vi-Br[b]	**13.1**	**10.8**	**10.4**
vi-NO$_2$[b]	**11.5**	**11.5**	**10.6**
viii-OMe	20.0	9.0	15.2
viii-Br	18.4	7.8	15.2
viii-NO$_2$	17.9	8.2	10.9

[a] See computational methods section for theoretical details. [b] These pathways have the lowest rate-limiting activation free energies of the eight stereochemically distinct possibilities.

increasingly EWGs in the salen ligand leads to an increasingly more compact coordination of the reactants in the rate-determining TS structure. Thus, the Al–O bond distances to the carbonyl group of the incoming cyclic ester are 1.929, 1.912, and 1.892 Å, respectively, for the complexes with *p*-MeO, -Br, and -NO$_2$ substituents, respectively. Concomitantly, the C–O distances for the forming bond between the carbonyl carbon and the ethoxide nucleophile are 1.784, 1.769, and 1.744 Å, respectively (the Al–O bond distance to the methoxide varies by less than 0.005 Å over the different substitutions). Thus, it appears that the more electrophilic Al center best stabilizes the incipient tetrahedral intermediate character in the TS structure, thereby effecting the observed rate acceleration.

While the predicted free energies of activation show a trend with respect to substitution that agrees well with experiment, they are considerably smaller in absolute magnitude than those measured experimentally. Comparison of the enthalpic and entropic contributions to the theoretical free energies relative to the experimental values indicates that theory predicts much smaller *enthalpies* of activation, but much larger *entropies* of activation. Such behavior might be associated with either or both of two phenomena. First, in the actual polymerization process, the growing polymer chain may associate with the catalyst, either through noncovalent interactions or through coordination of oxygen functionality to aluminum, and the requirement that the chain be displaced by CL would be expected to increase the enthalpy of activation and decrease the entropy of activation. Similarly, solvent toluene could enjoy particularly favorable π-stacking interactions with the aromatic rings of the salen ligand, for example, again introducing a larger enthalpy of activation and a less unfavorable entropy of activation (owing to solvent release) associated with reaction CL. In the absence of detailed (and impractical) simulations including solvent and an actual polymer chain, however, it is difficult to do more than speculate about these possibilities.

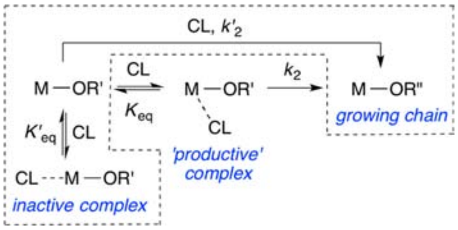

Figure 10. Proposed ROTEP mechanisms that yield the rate law described by eq 1. M = [(salen)Al] moiety.

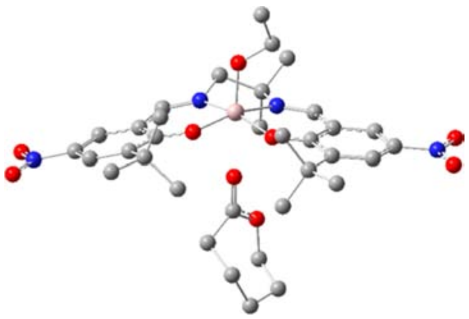

Figure 11. Unproductive complex of CL with *p*-NO$_2$-catalyst.

Also, as noted above, a key finding from the DFT calculations is *unfavorable* free energies for prereactive complexes that are implicated by the usual interpretation of the Michaelis–Menten equation (eq 1), wherein a pre-equilibrium substrate binding step (K_{eq}) is followed by a catalytic turnover step (k_2; Figure 10). To reconcile the experimentally observed rate law (eq 1) with the absence of such a binding step from the calculated reaction trajectories, we propose a different mechanism involving *substrate inhibition* (steps enclosed by dashed line in Figure 10, characterized by K'_{eq} and k'_2) that yields an experimental rate law indistinguishable from eq 1 (see Supporting Information for derivation). According to this mechanism, reversible substrate binding can be *non*productive, owing to formation of an *inactive* species. This species would be expected to be favored at high CL concentrations, resulting in rate retardation under these conditions (saturation kinetics). One such complex that can be imagined involves coordination of CL to Al trans to the alkoxide ligand, generating a complex that could not lead to intramolecular nucleophilic attack. Many such 6-coordinate Al(salen) complexes are known.[34] To specifically explore this possibility in our system, we computed the structure of the relevant complex for the *p*-NO$_2$ substituted salen case (Figure 11). It has a free energy that is 8.4 kcal/mol lower than any of the productively coordinated species presented in Tables 4 and 5. In addition, while not shown, we also located various van der Waals complexes of CL with the aromatic portions of the salen ligand that were also predicted to have lower free energies than productively coordinated complexes (adjacent to the alkoxide ligand). A quantitative measure of the inhibitory effect would require a statistical average over all nonproductive complexes, which is not practical in the absence of detailed molecular simulations. Nevertheless, the substrate inhibition mechanism (steps K'_{eq} and k'_2) is consistent with the experimental kinetics, and provides an alternative to the assumption in the pre-equilibrium mechanism that K_{eq} refers to productive coordination of substrate as a separate step prior to alkoxide insertion. Indeed, the substrate inhibition model represents a potentially important general phenomenon in ROTEP with catalysts for which both productive and unproductive coordination geometries of substrate and catalyst are available.

As a final, technical point related to the modeling, we note that use of the M06-L functional, with its well established ability to account for attractive medium-range electron correlation effects (sometimes informally referred to as “dispersion”, although that term really should only be used for longer-range attractive effects varying as r^{-6} with distance), is critical for the determination of accurate catalyst-CL complex geometries. When the 6-coordinate precursor structure corresponding to ***r-vi*** is reoptimized with the B3LYP functional, for example, which does *not* account for medium-range correlation effects, the bond distance between the carbonyl oxygen and the aluminum atom changes from the M06-L value of 2.18 Å to a value of 4.89 Å, i.e., the CL fully decoordinates.

SUMMARY AND CONCLUSIONS

Detailed kinetic studies of the polymerization of CL by salen-aluminum catalysts **2** (R = OMe, Br, or NO_2) supported by ligands with similar steric profiles but different electron donating characteristics revealed saturation behavior that fits to the rate eq 1. While K_{eq} varied only slightly with the electron donating properties of R (Hammett $\rho = +0.16(8)$), k_2 showed a more significant dependence reflected by $\rho = +1.4(1)$. These conclusions were buttressed by the dependencies of K_{eq} and k_2 with temperature that led to essentially invariant ΔG° values of ~0 kcal/mol for all catalysts (Table 2) and a discernible trend in $\Delta H^\ddagger$ of R = OMe > Br > NO_2 (Table 3). The observation of faster rates with EWGs on the supporting ligand agrees with the results of previous studies of ROTEP reactions catalyzed by related salen-aluminum complexes.[3,4]

The lowest energy reaction trajectories calculated by DFT (**r** and **s**-*vi*) have similarities to those proposed for ROTEP of LA stereoisomers by (*β*-diketiminate)Zn and -Sn catalysts,[35,36] in particular with respect to the first transition state structure that features incipient attack of the nucleophile to the lactone carbonyl that is bound to the metal ion. With respect to the effects of the remote ligand substituents, both the trend and the free energy of activation differences observed experimentally are reproduced in pathway *vi*. The greater Lewis acidity of the electron-deficient metal ion accelerates the reaction via transition state stabilization that involves increased bonding between the Al ion and the lactone carbonyl and between the nucleophilic alkoxide and the lactone carbonyl carbon.

Interestingly, DFT calculations indicated that a distinct CL adduct is not a free energy minimum on the reaction pathway, arguing against K_{eq} being associated with productive coordination of monomer according to the typical coordination–insertion mechanism (Figures 1 and 10). Instead, we propose that K_{eq} corresponds to “nonproductive” coordination of substrate that inhibits the reaction at high substrate concentrations, with k_2 thus encompassing both “productive” coordination and insertion steps that occur smoothly along the reaction trajectory. This attribution of saturation behavior to monomer inhibition has potentially significant implications for the interpretation of mechanistic studies of ROTEP catalysis and for the design of new catalysts. For example, we predict that catalysts for which nonproductive monomer coordination is prevented may be particularly efficient, particularly when high monomer concentrations are used (e.g., neat or in the melt).

EXPERIMENTAL SECTION

General Considerations. All reactions were carried out under an inert atmosphere using standard Schlenk and drybox techniques, unless otherwise indicated. Reagents were obtained from commercial suppliers and used as received unless otherwise indicated. CL was purified by distillation from CaH_2 and stored under N_2. Deuterated solvents were dried over CaH_2 or sodium, distilled under vacuum and stored under N_2. Protiated solvents were degassed and passed through a solvent purification system (Glass Contour, Laguna, CA) prior to use. ^1H and ^{13}C NMR spectra were recorded on a Varian VI-300 NMR spectrometer or a Bruker Avance III 500 MHz spectrometer equipped with a BBFO SmartProbe, and their chemical shifts (δ) for ^1H and ^{13}C spectra are referenced to residual protium in the deuterated solvent (for ^1H) and deuterated solvent itself (for ^{13}C). Chemical shifts for ^{27}Al NMR were externally referenced to aluminum *tris*(acetylacetonate) in toluene-d_8. 2-Hydroxy-3-(*tert*-butyl)-5-methoxybenzaldehyde,[37] 2-hydroxy-3-(*tert*-butyl)-5-bromobenzaldehyde,[38] and 2-hydroxy-3-(*tert*-butyl)-5-nitrobenzaldehyde[39] were synthesized according to literature procedures. Elemental analyses were performed by Complete Analysis Laboratories, Inc., Parsippany, NJ.

Ligand Syntheses. The benzaldehyde (H_2L^{OMe}: 7.7 g, 83% pure, 31 mmol; H_2L^{Br}: 1.40 g, 5.44 mmol; H_2L^{NO2}: 1.61 g, 88% pure, 6.35 mmol) was added to a round-bottom flask with the appropriate amount of absolute ethanol to give 0.63 M benzaldehyde. 2-Methylpropane-1,2-diamine (0.5 equiv) was added in one portion to the flask with stirring. A reflux condenser was added and the mixture was refluxed at 100 °C for 2 h, then allowed to cool to room temperature. The crude solution was placed in a −30 °C freezer overnight to induce precipitation of the protonated form of the ligand. After recovery by filtration washing with 40 mL of hexanes and in the case of H_2L^{Br}, recrystallization from dichloromethane and hexanes at −30 °C overnight, the solid product was placed in a vacuum oven overnight before bringing into the glovebox for metalation. Yield: H_2L^{OMe}: 5.62 g, 98%; H_2L^{Br}: 1.08 g, 35%; H_2L^{NO2}: 1.38 g, 87%). H_2L^{OMe}: ^1H NMR (500 MHz, $CDCl_3$) δ 13.95 (s, 1H, O*H*), 13.42 (s, 1H, O*H*), 8.35 (s, 1H, C*H*=N), 8.31 (s, 1H, C*H*=N), 6.96 (app t, *J* = 3.37 Hz, 2H, Ar*H*,), 6.60 (d, *J* = 3 Hz, 1H, Ar*H*), 6.58 (d, *J* = 3 Hz, 1H, Ar*H*), 3.76 (s, 3H, ArO*Me*), 3.75 (s, 3H, ArO*Me*), 3.72 (s, 2H, $NCH_2C(CH_3)_2N$), 1.44 (s, 6H, $NCH_2C(CH_3)_2N$), 1.42 (s, 9H, Ar*t*-*Bu*), 1.41 (s, 9H, Ar*t*-*Bu*); ^{13}C NMR (125 MHz, $CDCl_3$) δ 167.26, 162.37, 155.32, 155.13, 151.31, 151.24, 139.15, 139.14, 118.61, 118.42, 118.09, 117.99, 111.72, 111.62, 70.57, 60.28, 55.91, 35.14, 35.12, 29.41, 29.39, 25.69. Anal. Calcd for $C_{28}H_{40}N_2O_2$: C, 71.76; H, 8.60; N, 5.98. Found: C, 71.73; H, 8.57; N, 5.98.

H_2L^{Br}: ^1H NMR (500 MHz, $CDCl_3$) δ 14.39 (s, 1H, O*H*), 13.83 (s, 1H, O*H*), 8.29 (s, 1H, C*H*=N), 8.25 (s, 1H, C*H*=N), 7.37 (d, *J* = 2.5 Hz, 1H, Ar*H*), 7.36 (d, *J* = 2 Hz, 1H, Ar*H*), 7.23 (d, *J* = 2.5 Hz, 1H, Ar*H*), 7.20 (d, *J* = 2.5 Hz, 1H, Ar*H*), 3.72 (s, 2H, $NCH_2C(CH_3)_2N$), 1.43 (s, 6H, $NCH_2C(CH_3)_2N$), 1.40 (s, 18H, Ar*t*-*Bu*); ^{13}C NMR (125 MHz, $CDCl_3$) δ 166.37, 161.45, 159.97, 159.69, 140.32, 140.29, 132.63, 132.39, 131.98, 131.84, 119.98, 119.91, 109.90, 109.70, 70.35, 60.45, 35.25, 35.23, 29.25, 25.55. Anal. Calcd for $C_{26}H_{34}Br_2N_2O_2$: C, 55.14; H, 6.05; N, 4.95. Found: C, 55.08; H, 6.09; N, 4.90.

H_2L^{NO2}: ^1H NMR (500 MHz, $CDCl_3$) δ 15.68 (s, 1H, O*H*), 14.94 (s, 1H, O*H*), 8.43 (app s, 2H, C*H*=N), 8.23 (d, *J* = 2.5 Hz, 1H, Ar*H*), 8.20 (d, *J* = 2.5 Hz, 1H, Ar*H*), 8.13 (d, *J* = 2.5 Hz, 1H, Ar*H*), 8.12 (d, *J* = 3 Hz, 1H, Ar*H*), 3.82 (s, 2H, $NCH_2C(CH_3)_2N$), 1.54 (s, 2H, $NCH_2C(CH_3)_2N$), 1.52 (s, 6H, $NCH_2C(CH_3)_2N$), 1.43 (s, 9H, Ar*t*-*Bu*), 1.42 (s, 9H, Ar*t*-*Bu*); ^{13}C NMR (125 MHz, $CDCl_3$) δ 168.59, 167.12, 166.73, 161.83, 140.26, 139.93, 139.02, 126.90, 126.44, 125.39, 117.19, 116.78, 69.47, 60.47, 70.35, 60.45, 35.45, 35.41, 29.07, 25.45. Anal. Calcd for $C_{26}H_{34}N_4O_6$: C, 62.63; H, 6.87; N, 11.24. Found: C, 62.54; H, 6.67; N, 11.15.

Aluminum Complexes (2). In a nitrogen-filled glovebox, equimolar amounts of the pro-ligand (H_2L^{OMe}: 0.596 g, 1.27 mmol; H_2L^{Br}: 0.719 g, 1.27 mmol; H_2L^{NO2}: 0.778 g, 1.56 mmol) and aluminum tris(*iso*-propoxide) were added to an oven-dried 15 mL screw cap glass vessel. Toluene (3 mL) was added, and the vessel was equipped with a stir bar, sealed, and removed from the glovebox. The sealed vessel was heated to 90 °C for 3 days, after which time it was cooled to room temperature and returned to the glovebox. Toluene was removed in vacuo from the homogeneous solutions to yield the products as a colored powder (R = OMe: bright yellow; R = Br: yellow; R = NO$_2$: light brown). The powder was triturated with pentane and collected by filtration through a glass frit. In the cases of R = Br and NO$_2$, the solid was dried on a vacuum line overnight and used without further purification. The resulting solid in the case of R = OMe was recrystallized from toluene/pentane at −40 °C, and the crystals were dried overnight on a vacuum line before use. Yields: R = OMe: 0.591 g (84%); R = Br: 0.712 g (86%); R = NO$_2$: 0.879 g (97%).

R = OMe: ^{1}H NMR (500 MHz, toluene-d_8) δ 7.93 (s, 1H, C*H*═N), 7.45 (s, 1H, C*H*═N), 7.38 (d, *J* = 3 Hz, 1H, Ar*H*), 7.36 (d, *J* = 3 Hz, 1H, Ar*H*), 6.38 (d, *J* = 3 Hz, 1H, Ar*H*), 6.27 (d, *J* = 2.6 Hz, 1H, Ar*H*), 4.15 (q, *J* = 6 Hz, 1H, OC*H*(CH$_3$)$_2$), 3.75 (d, *J* = 12 Hz, 1H, NC*H*$_2$C(CH$_3$)$_2$N), 3.52 (s, 3H, ArO*Me*), 3.49 (s, 3H, ArO*Me*), 2.47 (d, *J* = 12 Hz, 1H, NC*H*$_2$C(CH$_3$)$_2$N), 1.76 (s, 9H, Ar*t*-*Bu*), 1.74 (s, 9H, Ar*t*-*Bu*), 1.17 (d, *J* = 6.0 Hz, 3H, OCH(C*H*$_3$)$_2$), 1.11 (s, 3H, NCH$_2$C(C*H*$_3$)$_2$N), 1.10 (d, *J* = 6.3 Hz, 3H, OCH(C*H*$_3$)$_2$), 0.62 (s, 3H, NCH$_2$C(C*H*$_3$)$_2$N); ^{27}Al NMR (130 MHz, toluene-d_8) δ 35.23. Anal. Calcd for $C_{31}H_{45}AlN_2O_5$: C, 67.37; H, 8.21; N, 5.07. Found: C, 67.43; H, 8.23; N, 4.98.

R = Br: ^{1}H NMR (500 MHz, toluene-d_8) δ 7.70 (d, *J* = 2.7 Hz, 1H, Ar*H*), 7.69 (d, *J* = 2.8 Hz, 1H, Ar*H*), 7.64 (s, 1H, C*H*═N), 7.18 (s, 1H C*H*═N), 6.97 (d, *J* = 2.6 Hz, 1H, Ar*H*), 6.91 (d, *J* = 2.6 Hz, 1H, Ar*H*), 4.05 (q, *J* = 5.9 Hz, 1H, OC*H*(CH$_3$)$_2$), 3.65 (d, *J* = 12.3 Hz, 1H, NC*H*$_2$C(CH$_3$)$_2$N), 2.39 (d, *J* = 12.2 Hz, 1H, NC*H*$_2$C(CH$_3$)$_2$N), 1.65 (s, 9H, Ar*t*-*Bu*), 1.63 (s, 9H, Ar*t*-*Bu*), 1.15 (d, *J* = 6.0 Hz, 3H, OCH(C*H*$_3$)$_2$), 1.06 (d, *J* = 6.3 Hz, 3H, OCH(C*H*$_3$)$_2$), 1.06 (s, 3H, NCH$_2$C(C*H*$_3$)$_2$N), 0.57 (s, 3H, NCH$_2$C(C*H*$_3$)$_2$N); ^{27}Al NMR (130 MHz, toluene-d_8) δ 34.11. Anal. Calcd for $C_{29}H_{39}AlBr_2N_2O_3$: C, 53.55; H, 6.04; N, 4.31. Found: C, 53.60; H, 6.08; N, 4.31.

R = NO$_2$: ^{1}H NMR (500 MHz, toluene-d_8) δ 8.49 (d, *J* = 2.1 Hz, 1H, Ar*H*), 8.48 (d, *J* = 2.3 Hz, 1H, Ar*H*), 7.92 (d, *J* = 2.4 Hz, 1H, Ar*H*), 7.76 (d, *J* = 2.3 Hz, 1H, Ar*H*), 7.66 (s, 1H, C*H*═N), 7.10 (s, 1H, C*H*═N), 3.96 (q, *J* = 5.7 Hz, 1H, OC*H*(CH$_3$)$_2$), 3.59 (d, *J* = 12.4 Hz, 1H, NC*H*$_2$C(CH$_3$)$_2$N), 2.43 (d, *J* = 12.3 Hz, 1H, NC*H*$_2$C(CH$_3$)$_2$N), 1.62 (s, 9H, Ar*t*-*Bu*), 1.60 (s, 9H, Ar*t*-*Bu*), 1.10 (d, *J* = 5.8 Hz, 3H, OCH(C*H*$_3$)$_2$), 1.04 (s, 3H, NCH$_2$C(C*H*$_3$)$_2$N), 1.03 (d, *J* = 6.3 Hz, 3H, OCH(C*H*$_3$)$_2$), 0.58 (s, 3H, NCH$_2$C(C*H*$_3$)$_2$N); ^{27}Al NMR (130 MHz, toluene-d_8) δ 33.07. Anal. Calcd for $C_{29}H_{39}AlN_4O_7$: C, 59.78; H, 6.75; N, 9.62. Found: C, 59.78; H, 6.78; N, 9.62.

^{1}H NMR Kinetics. A representative procedure for the kinetic studies is described. To an oven-dried NMR tube in a nitrogen-filled glovebox, 500 μL of a stock solution of catalyst in toluene-d_8 (0.0092 M) and 10 μL of the internal standard bis(*para*-trimethylsilyl)benzene in toluene-d_8 (0.28 M) were added. The NMR tube was capped with a septum and wrapped with parafilm. A gastight syringe was loaded with 190 μL of ε-caprolactone (CL) stock solution (7.4 M), also in toluene-d_8. The target final concentrations of catalyst, internal standard, and CL were 0.0062 M, 0.004 M, and 2 M, respectively. The gastight syringe containing CL was inserted into a rubber septum to prevent air contamination during the experiment setup. The NMR tube and syringe were removed from the glovebox and brought to the spectrometer. The temperature on the NMR spectrometer (300 MHz Varian Inova) was calibrated using an ethylene glycol standard. A ^{1}H NMR spectrum was taken of the initial catalyst and internal standard solution before addition of CL with a relaxation time of 10 s and a 30° pulse width to ensure complete relaxation for quantitative integrations to determine catalyst concentration. Next, the tube was ejected from the spectrometer and CL was injected through the septum into the NMR tube, and the time between CL injection and start of the ^{1}H NMR data acquisition was recorded in minutes. The contents of the tube were well mixed before reinserting the NMR tube into the spectrometer. Again, a relaxation time of 10 s and a 30° pulse width were used for quantitative purposes, and an arrayed set of spectra were taken every 96, 192, or 384 s with 8, 16, or 32 scans, respectively, spin rate of 16 Hz, acquisition time 2 s, and maximum gain. The arrayed experiment was allowed to proceed until polymerization had completed, as indicated by the disappearance of the CL peaks. For each catalyst, four temperatures were carefully chosen, and three reactions were repeated at each temperature. The obtained arrayed NMR data were phased and baseline corrected in Mestrenova (http://mestrelab.com/) before being integrated by the same program. The integrations were recorded and entered into an Excel spreadsheet. Absolute concentrations of all species as a function of time were computed relative to the concentration of internal standard. Reaction time was calculated in seconds from the known length of time per spectrum and the time between CL injection and the start of the ^{1}H NMR data acquisition. The concentration vs time data obtained from the ^{1}H NMR data were input into the COPASI program and fit to eq 1 to obtain K_M and k_2 values. COPASI fitting plots (concentration vs time) are shown in Supporting Information, Figure S1. The reaction rates were calculated by eq 1 and plotted as a function of concentration, as shown in Supporting Information, Figure S2. Kinetic parameters determined by COPASI are listed in Supporting Information, Table S1. All linear and nonlinear curve fits were performed using Graphpad Prism software. In a test of the significance of possible viscosity effects on the kinetics performed in the NMR tubes, a stirred polymerization using **2** (R = NO$_2$) at 298 K (average temperature inside nitrogen-filled glovebox over the course of the reaction) with $[\mathbf{2}\ (\mathrm{R} = \mathrm{NO_2})]_{\mathrm{tot}}$ = 5.8 mM and $[\mathrm{CL}]_0$ = 2 M (total volume 5 mL). Aliquots were removed at selected time points for NMR analysis, which revealed rate parameters similar to those seen in the NMR tube experiments (see Supporting Information for details).

Density Functional Calculations. All stationary molecular geometries were fully optimized in the gas phase at the M06-L level of DFT[40] employing the 6-31+G(d,p) basis set[41] in the Gaussian09 electronic structure program suite.[42] The nature of individual stationary points, that is, their characterization as either minima or TS structures, was verified by the computation of analytical vibrational frequencies. These same calculations, within the conventional ideal-gas, rigid-rotator, quantum-mechanical harmonic-oscillator (QMHO) approximation,[43] permitted the computation of thermal contributions to 323.15 K free energies. To compensate for errors in the QMHO approximation when applied to very low-frequency normal modes, vibrational frequencies below 50 cm^{-1} were replaced by values of 50 cm^{-1} (the quasi-harmonic approximation[44]). The effects of toluene as solvent were included through calculations at the same level of theory using the SMD quantum-mechanical continuum solvation model for the gas-phase optimized structures. In select instances, we explored the influence of reoptimization of the geometries including solvation and determined that the effects were small, and insofar as geometric convergence was considerably slower with the solvation model included, we restricted our consideration to gas-phase structures. Final, best-estimate composite free energies in solution were computed by replacing the M06-L/6-31+G(d,p) gas-phase electronic energies with single-point electronic energies computed using the M06-2X density functional[45] and the 6-311+G(d,p) basis set.[46] Minima connected through individual TS structures were determined by displacing the geometries of TS structures by small amounts in both directions along their corresponding reaction coordinates and permitting the resulting structures to optimize to their associated minima.

■ ASSOCIATED CONTENT

Ⓢ Supporting Information

Experimental data, analysis (comparison to alternative rate law fits, error evaluation), and theory details (PDF). This material is available free of charge via the Internet at http://pubs.acs.org.

■ AUTHOR INFORMATION

Corresponding Authors

*E-mail: cramer@umn.edu (C.J.C.).
*E-mail: wtolman@umn.edu (W.B.T.).

Notes

The authors declare no competing financial interest.

■ ACKNOWLEDGMENTS

This work was supported by the Center for Sustainable Polymers at the University of Minnesota, a National Science Foundation (NSF) supported Center for Chemical Innovation (CHE-1136607), and by NSF grants to D.J.M. and C.J.C. (CHE-0952054), an NSF graduate research fellowship to M.O.M. (Grant 00006595), a CONACYT postdoctoral grant to H. V.-L. (Grant 186695), and UM Lando and Heisig grants in support of undergraduate student research (Y.D. and M.A.J.).

■ REFERENCES

(1) (a) Gandini, A. *Macromolecules* **2008**, *41*, 9491−9504. (b) *Renewable Polymers: Synthesis, Processing, and Technology*; Mittal, V., Ed.; John Wiley & Sons and Scrivener Publishing: Hoboken, NJ, and Salem, MA, 2012.

(2) (a) Drumright, R. E.; Gruber, P. R.; Henton, D. E. *Adv. Mater.* **2000**, *12*, 1841−1846. (b) Wu, J.; Yu, T.-L.; Chen, C.-T.; Lin, C.-C. *Coord. Chem. Rev.* **2006**, *250*, 602−626. (c) Dechy-Cabaret, O.; Martin-Vaca, B.; Bourissou, D. *Chem. Rev.* **2004**, *104*, 6147−6176. (d) O'Keefe, B. J.; Hillmyer, M. A.; Tolman, W. B. *J. Chem. Soc., Dalton Trans.* **2001**, 2215−2224. (e) Kamber, N. E.; Jeong, W.; Pratt, R. C.; Lohmeijer, B. G. G.; Waymouth, R. M.; Hedrick, J. L. *Chem. Rev.* **2007**, *107*, 5813−5840.

(3) Hormnirun, P.; Marshall, E. L.; Gibson, V. C.; Pugh, R. I.; White, A. J. P. *Proc. Natl. Acad. Sci. U.S.A.* **2006**, *103*, 15343−15348.

(4) Nomura, N.; Ishii, R.; Yamamoto, Y.; Kondo, T. *Chem.—Eur. J.* **2007**, *13*, 4433−4451.

(5) Wang, Y.; Ma, H. *Chem. Commun.* **2012**, *48*, 6729−6731.

(6) Gregson, C. K. A.; Blackmore, I. J.; Gibson, V. C.; Long, N. J.; Marshall, E. L.; White, A. J. P. *Dalton Trans.* **2006**, 3134−3140.

(7) Wu, J.; Chen, Y.-Z.; Hung, W.-C.; Lin, C.-C. *Organometallics* **2008**, *27*, 4970−4978.

(8) Alcazar-Roman, L. M.; O'Keefe, B. J.; Hillmyer, M. A.; Tolman, W. B. *Dalton Trans.* **2003**, 3082−3087.

(9) Ding, K.; Miranda, M. O.; Moscato-Goodpaster, B.; Ajellal, N.; Breyfogle, L. E.; Hermes, E. D.; Schaller, C. P.; Roe, S. E.; Cramer, C. J.; Hillmyer, M. A.; Tolman, W. B. *Macromolecules* **2012**, *45*, 5387−5396.

(10) (a) Cozzi, P. G. *Chem. Soc. Rev.* **2004**, *33*, 410−421. (b) Che, C. *Coord. Chem. Rev.* **2003**, *242*, 97−113.

(11) Spassky, N.; Wisniewski, M.; Pluta, C.; Borgne, A. L. *Macromol. Chem. Phys.* **1996**, *197*, 2627−2637.

(12) Ovitt, T. M.; Coates, G. W. *J. Am. Chem. Soc.* **1999**, *121*, 4072−4073.

(13) Ovitt, T. M.; Coates, G. W. *J. Polym. Sci., Part A: Polym. Chem.* **2000**, 4686−4692.

(14) Ovitt, T. M.; Coates, G. W. *J. Am. Chem. Soc.* **2002**, *124*, 1316−1326.

(15) Radano, C. P.; Baker, G. L.; Smith, M. R., III *J. Am. Chem. Soc.* **2000**, *122*, 1552−1553.

(16) Majerska, K.; Duda, A. *J. Am. Chem . Soc.* **2004**, *126*, 1026−1027.

(17) Breteler, M. R. T.; Zhong, Z.; Dijkstra, P. J.; Palmans, A. R. A.; Peeters, J.; Feijen, J. *J. Polym. Sci. A Polym. Chem.* **2006**, *45*, 429−436.

(18) Zhong, Z.; Dijkstra, P. J.; Feijen, J. *J. Am. Chem . Soc.* **2003**, *125*, 11291−11298.

(19) Yang, J.; Yu, Y.; Li, Q.; Li, Y.; Cao, A. *J. Polym. Sci. A: Polym. Chem.* **2004**, *43*, 373−384.

(20) Chisholm, M. H.; Patmore, N. J.; Zhou, Z. *Chem. Commun.* **2005**, 127−129.

(21) Chisholm, M. H.; Gallucci, J. C.; Quisenberry, K. T.; Zhou, Z. *Inorg. Chem.* **2008**, *47*, 2613−2624.

(22) van der Meulen, I.; Gubbels, E.; Huijser, S.; Sablong, R. l.; Koning, C. E.; Heise, A.; Duchateau, R. *Macromolecules* **2011**, *44*, 4301−4305.

(23) Pepels, M. P. F.; Bouyahyi, M.; Heise, A.; Duchateau, R. *Macromolecules* **2013**, *46*, 4324−4334.

(24) Cross, E. D.; Allan, L. E. N.; Decken, A.; Shaver, M. P. *J. Polym. Sci. Part A: Polym. Chem.* **2012**, *51*, 1137−1146.

(25) Du, H.; Pang, X.; Yu, H.; Zhuang, X.; Chen, X.; Cui, D.; Wang, X.; Jing, X. *Macromolecules* **2007**, *40*, 1904−1913.

(26) Atwood, D. A.; Harvey, M. J. *Chem. Rev.* **2001**, *101*, 37−52.

(27) Addison, A. W.; Rao, T. N.; Reedijk, J.; Rijn, J. V.; Verschoor, G. C. *J. Chem. Soc., Dalton Trans.* **1984**, 1349−1356.

(28) Hoops, S.; Sahle, S.; Gauges, R.; Lee, C.; Pahle, J.; Simus, N.; Singhal, M.; Xu, L.; Mendes, P.; Kummer, U. *Bioinformatics* **2006**, *22*, 3067−3074.

(29) Blackmond, D. *Angew. Chem., Int. Ed.* **2005**, *44*, 4302−4320.

(30) Hansch, C.; Leo, A.; Taft, R. W. *Chem. Rev.* **1991**, *91*, 165−195.

(31) Values for the rate constants k_2 and K_{eq} at temperatures that were not experimentally measured but presented in Figure 6 were obtained by extrapolating the thermodynamic parameters from the Erying (k_2) and van't Hoff (K_M) plots (see Tables 2 and 3 for thermodynamic parameters).

(32) Talarico, G.; Barone, V.; Joubert, L.; Adamo, C. *Int. J. Quantum Chem.* **2003**, *91*, 474−482.

(33) Marenich, A. V.; Jerome, S. V.; Cramer, C. J.; Truhlar, D. G. *J. Chem. Theor. Comput.* **2012**, *8*, 527−541.

(34) A search of the Cambridge Crystallographic Database (v. 5.34) revealed >20 such structures. Some illustrative examples: (a) Jegier, J. A.; Muñoz-Hernández, M.-Á.; Atwood, D. A. *J. Chem. Soc., Dalton Trans.* **1999**, 2583−2588. (b) Muñoz-Hernández, M.-Á.; McKee, M. L.; Keizer, T. S.; Yearwood, B. C.; Atwood, D. A. *J. Chem. Soc., Dalton Trans.* **2002**, 410−414. (c) Getzler, Y. D.; Mahadevan, V.; Lobkovsky, E. B.; Coates, G. W. *Pure Appl. Chem.* **2004**, *76*, 557−564.

(35) Marshall, E. L.; Gibson, V. C.; Rzepa, H. S. *J. Am. Chem. Soc.* **2005**, *126*, 6048−6051.

(36) Dove, A. P.; Gibson, V. C.; Marshall, E. L.; Rzepa, H. S.; White, A. J. P.; Williams, D. J. *J. Am. Chem. Soc.* **2006**, *128*, 9834−9843.

(37) Kurahashi, T.; Fujii, H. *J. Am. Chem. Soc.* **2011**, *133*, 8307−8316.

(38) Cavazzini, M.; Manfredi, A.; Montanari, F.; Quici, S.; Pozzi, G. *Eur. J. Org. Chem.* **2001**, 4639−4649.

(39) Braun, M.; Fleischer, R.; Mai, B.; Schneider, M.-A.; Lachenicht, S. *Adv. Synth. Catal.* **2004**, *346*, 474−482.

(40) Zhao, Y.; Truhlar, D. G. *J. Chem. Phys.* **2006**, *125*, 194101.

(41) Hehre, W. J.; Radom, L.; Schleyer, P. v. R.; Pople, J. A. *Ab Initio Molecular Orbital Theory*; Wiley: New York, 1986.

(42) Frisch, M. J. et al. *Gaussian 09*, Revision C.01; Gaussian, Inc.: Wallingford, CT, 2010. See Supporting Information for full reference.

(43) Cramer, C. J. *Essentials of Computational Chemistry: Theories and Models*, 2nd ed.; John Wiley & Sons: Chichester, U.K., 2004.

(44) Ribeiro, R. F.; Marenich, A. V.; Cramer, C. J.; Truhlar, D. G. *J. Phys. Chem. B* **2011**, *115*, 14556−14562.

(45) Zhao, Y.; Truhlar, D. G. *Theor. Chem. Acc.* **2008**, *120*, 215−241.

(46) Hehre, W. J.; Radom, L.; Schleyer, P. v. R.; Pople, J. A. *Ab Initio Molecular Orbital Theory*; Wiley: New York, 1986.